Characterization, Reconstruction and Transport Properties of Vosges Sandstones

J.-C. Moulu, F. Kalaydjian, C. D. Tsakiroglou, V. N. Burganos, A. C. Payatakes, J. Yao, J.-F. Thovert, P.-M. Adler

CHARACTERIZATION, RECONSTRUCTION AND TRANSPORT PROPERTIES OF VOSGES SANDSTONES

J. YAO and J.-F. THOVERT

LPTM[1]

P.-M. ADLER

IPGP[2]

C.D. TSAKIROGLOU, V.N. BURGANOS and A.C. PAYATAKES

Institute of Chemical Engineering and High Temperature Chemical Processes[3]

J.-C. MOULU and F. KALAYDJIAN

Institut français du pétrole[4]

(1) SP2MI, BP 179, 86960 - Futuroscope Cedex - France

(2) 4, place Jussieu, 75252 - Paris Cedex 05 - France

(3) Foundation for Research and Technology - Hellas, PO Box 1414, 26500 Patras - Greece

(4) 1 et 4, avenue de Bois-Préau, 92852 Rueil-Malmaison Cedex - France

CARACTÉRISATION, RECONSTRUCTION ET PROPRIÉTÉS DE TRANSPORT DES GRÈS DES VOSGES

Dans cet article, nous présentons une étude approfondie d'échantillons de grès des Vosges. La géométrie de ces milieux est analysée en utilisant des coupes sériées. Puis des échantillons aléatoires sont reconstruits en accord avec les propriétés géométriques statistiques mesurées. Enfin, les propriétés macroscopiques de transport sont déduites des solutions numériques dans les échantillons reconstruits des équations locales qui régissent les transports correspondants, et elles sont comparées aux mesures disponibles. La pénétration de mercure dans les échantillons est modélisée et les résultats relatifs aux distributions de pores sont comparés à ceux obtenus sur les coupes sériées.

CHARACTERIZATION, RECONSTRUCTION AND TRANSPORT PROPERTIES OF VOSGES SANDSTONES

A thorough study of Vosges sandstone samples is presented in this work. First, the geometry of these porous media is analyzed using serial thin sections. Then, random numerical samples are reconstructed according to the measured statistical geometrical parameters. Finally, the macroscopic transport properties are determined from the numerical solutions in the reconstructed samples of the local equations governing the corresponding transport phenomena and compared to available experimental data. Mercury intrusion in the simulated media is modelled and pore size distribution results are compared with those obtained from serial tomography.

CARACTERIZACIÓN, RECONSTRUCCIÓN Y PROPIEDADES DE TRANSPORTE DE GRES DE LOS VOSGOS

Se presenta en este artículo un estudio detallado de muestras de gres de los Vosgos. La geometría de estos medios se analiza utilizando para ello secciones seriadas. Acto seguido, las muestras aleatorias se reconstruyen en concordancia con las propiedades geométricas estadísticas objeto de las medidas. Finalmente, las propiedades macroscópicas de transporte se deducen de soluciones digitales en las muestras reconstruidas de las ecuaciones locales que gobiernan los transportes correspondientes y, asimismo se comparan con las mediciones disponibles. La penetración de mercurio en las muestras se modeliza y los resultados relativos a las distribuciones de poro se comparan a su vez con aquellos obtenidos en las secciones seriadas.

INTRODUCTION

The study of structural and transport properties of oil reservoir rocks is of critical importance for the efficient design of enhanced recovery processes. The geometrical and topological analysis of the pore structure of Vosges sanstones as well as the prediction of their most significant transport coefficients, such as permeability, diffusivity, and dispersivity, are the main goals of the present work and are implemented through a combination of simulation and experimental techniques.

The measurement of the relevant geometrical parameters on the experimental samples is described in Section 1. Two sets of serial thin sections were analyzed, composed of 6 (3A1) and 45 (2A1) sections from two plugs of Vosges sandstone. Two statistical properties of the pore space are measured, namely porosity and autocorrelation function. For each data set, the various sections are shown to be isotropic and to possess very similar autocorrelation functions, whereas their porosities vary slightly.

The reconstruction procedure is presented in Sections 2 and 3. It is shown how to generate a three-dimensional random porous medium with a given porosity and a given correlation function. The medium is made of elementary cubes which are filled by solid or liquid. It can be generated in two steps starting from independent Gaussian variables $X(\boldsymbol{x})$. Linear combinations of these variables yield a population $Y(\boldsymbol{x})$ which is still Gaussian but correlated; the correlation depends upon the set of coefficients $\bar{a}$ of the linear combinations. This population is then transformed into a discrete population $Z(\boldsymbol{x})$ which takes only two values, 0 and 1; this transformation is such that the average value of $Z(\boldsymbol{x})$ is automatically equal to the porosity.

In order to generate a given porous medium, one can first solve an inverse problem which consists of a two-step determination of the coefficients $\bar{a}$. Once these coefficients have been determined, artificial media can be generated at will starting from an arbitrary seed; one can also make use of an alternative and numerically more efficient method. Then, the coefficients $\bar{a}$ are not obtained explicitly and the field $Y(\boldsymbol{x})$ is built by operating in the Fourier space.

The results of the reconstruction are presented and discussed in Section 4. Average values of the correlation function and of the porosity were used as input data. Two- and three-dimensional visualizations of several reconstructed samples are presented. Then, the macroscopic transport properties of these reconstructed media are derived by solving numerically the differential equations governing the transport at the micro-scale. For instance, the permeability is derived from the velocity field obtained by solving the continuity and Stokes equations with the no-slip condition at the solid wall. This approach is applied to various transport processes for both sets of data.

The local problems to be solved are presented in Section 5, along with the methods of solution. The results of the simulations are presented and discussed in Section 6. The permeability and conductivity tensors have been computed and averaged over several reconstructed samples for each set of data. One set yields significantly larger than average transport coefficients, owing to its larger porosity and correlation length. The dispersion has been studied with the second set of data, by deriving the longitudinal dispersion coefficient as a function of the Peclet number *Pe*, for several reconstructed media with different sizes. A power-law with an exponent $\alpha \approx 1.7$ is obtained in every case.

Finally, Section 7 is devoted to the simulation of a mercury porosimetry experiment. The numerical method is briefly described and an application to a reconstructed sample is presented. The result is typical of the experimental curves for sandstones.

1 MEASUREMENTS

Measurements of the experimental porosity and correlation function were performed on two sets of serial cross-sections from two plugs of Vosges sandstone, obtained in the following fashion. A *double-pore casting* technique is used prior to serial tomography. This technique is a variance of similar techniques reported in the literature (see, for instance, Straley and Minnis, 1983; Lin and Hamasaki, 1983, Yadav *et al.*, 1987). The trapped fluids are first removed from the samples using an organic solvent. The porous medium is then dried, heated with Wood's metal, pressurized at 70 atm, and then cooled slowly to room temperature. The *single-pore cast* thus obtained is pelletised and the solid phase is dissolved using hydrofluoric acid. Following removal of trapped fluids and sample drying once again, a 4-component epoxy resin is injected into the Wood's metal matrix. The sample is pressurized at 50 atm and heated slightly (below 50°) to achieve controlled resin polymerisation. Cooling down to room temperature yields the final *double-pore cast*.

Subsequently, a number of serial sections were obtained (60 for sample 2A1, 10 for sample 3A1) using a special microtome. The setup is equipped with a section alignment device which uses a fixed frame of reference. Image grabbing and digitisation of each serial section were carried out in a highly automated manner. Each section is described by a 500 × 482 matrix of binary pixels, which take the values 0 or 1 in the solid or pore phases, respectively. The physical dimension of these pixels is 2.04 μm in both directions. This representation is a discrete definition of the phase function

$$Z(\boldsymbol{x}) = \begin{cases} 1 & \text{if } \boldsymbol{x} \text{ belongs to the pore space} \\ 0 & \text{otherwise} \end{cases} \quad (1)$$

where x is the position vector with respect to an arbitrary origin.

The six sections of set (3A1) are regularly spaced by 10 μm. They are displayed in Figure 1. Visual examination of the superposition of the images of Figure 1 reveals that there is a strong correlation between two successive frames, but that they are slightly shifted. A significant part of this shift is caused by the fact that the pore walls are not normal to the plane of the sections. The rest is caused by minute random errors in positioning the sample. The absolute value of this shift is generally very small (≤100 μm), but still represents a significant part of the overall frame size (≈ 1 mm). The shift of the sixth image with respect to the fifth one is somewhat larger (≈ 200 μm). However, the orientation of the x and y axes seems identical in all cases.

The porosity ε and the correlation $R_z(\boldsymbol{u})$ can be defined by the statistical averages (which are denoted by brackets $< \cdot >$)

$$\varepsilon = \langle Z(\boldsymbol{x}) \rangle \quad (2a)$$

$$R_z(\boldsymbol{u}) = \langle (Z(\boldsymbol{x}) - \langle Z \rangle)(Z(\boldsymbol{x} + \boldsymbol{u}) - \langle Z \rangle) \rangle / (\varepsilon - \varepsilon^2) \quad (2b)$$

where $u = \|u\|$. Notice that $(\varepsilon - \varepsilon^2)$ in (2b) equals var (Z) since $Z^2(\boldsymbol{x}) = Z(\boldsymbol{x})$.

These two quantities were measured for each section with image analysis. The porosity is obtained with a simple summation. The results are listed in Table 1. Despite the proximity of the successive cross-sections, and the strong correlation resulting from it, the porosity values observed on the various sections are somewhat scattered, in the range $0.20 \backsim 0.27$ around the average value 0.231. In order to check the homogeneity of the experimental sample, the porosity of each half-image was also measured. We denote by ε_1 (resp. ε_2) the porosity of the left (resp. right) half of the frames. The data in Table 1 reveal a definite trend, with a 0.075 difference between the averages of ε_1 and ε_2, larger than the standard deviation of ε, ε_1 or ε_2 . The overall porosity of the sample had also been measured previously and found equal to $\varepsilon = 0.21$.

The correlation function (2b) was evaluated for each section of set (3A1) by using standard translation and intersection routines. The increment $\boldsymbol{u}$ was varied by steps of one pixel; in order to check the isotropy of the medium, the direction of $\boldsymbol{u}$ was set along the x and y axes successively. The results are shown in Figure 2. The correlation functions of the six frames are shown in (a) for the x direction, in (b) for the y direction, and the averages over both directions for each frame are shown in (c). Clearly, the various sections yield very similar and isotropic correlation functions. This is in agreement with the statement made in previous works (Adler *et al.*, 1990; Sallès *et al.*, 1993a) that for a given type of material the correlation is not a sensitive function of the porosity. Note that the correlation function (2b) is defined for a statistically stationary medium. Inhomogeneities at the sample scale, like the difference between ε_1 and ε_2, result often in a noisy function R_z. Such problems do not arise here, and the various sections yield very similar correlation functions, whatever the value of $\varepsilon_1 - \varepsilon_2$.

The second set of experimental data consists of 45 successive sections, numbered from 1 to 45, from the same plug of Vosges sandstone (2A1). Each image consists of 500 × 482 binary pixels, whose dimensions are $p_x = p_y = 2.04$ μm. The successive sections are regularly separated by a spacing $p_z = 7.3$ μm. Only five of these 45 images, namely those with numbers (1, 10, 20, 30, 40) are shown in Figure 3. In the following, we refer to these as the subset of data for (2A1). They span most of the complete set, and owing to their wide separation (73 μm) they appear visually uncorrelated. The same processing as that followed for the first sample (3A1) was applied.

The porosity was measured on each image and half-image, yielding the values of Table 2. The average porosity $\varepsilon = 0.164$ is somewhat lower than that for sample 3A1 ($\varepsilon = 0.21$), but the standard deviation of the measurements on each image is comparable (≈ 10% in both cases). Again, the porosity ε_1 on the left-hand half-images is generally slightly larger than ε_2 measured on the right-hand halves, but less so than for sample (3A1). The average difference amounts to 0.022.

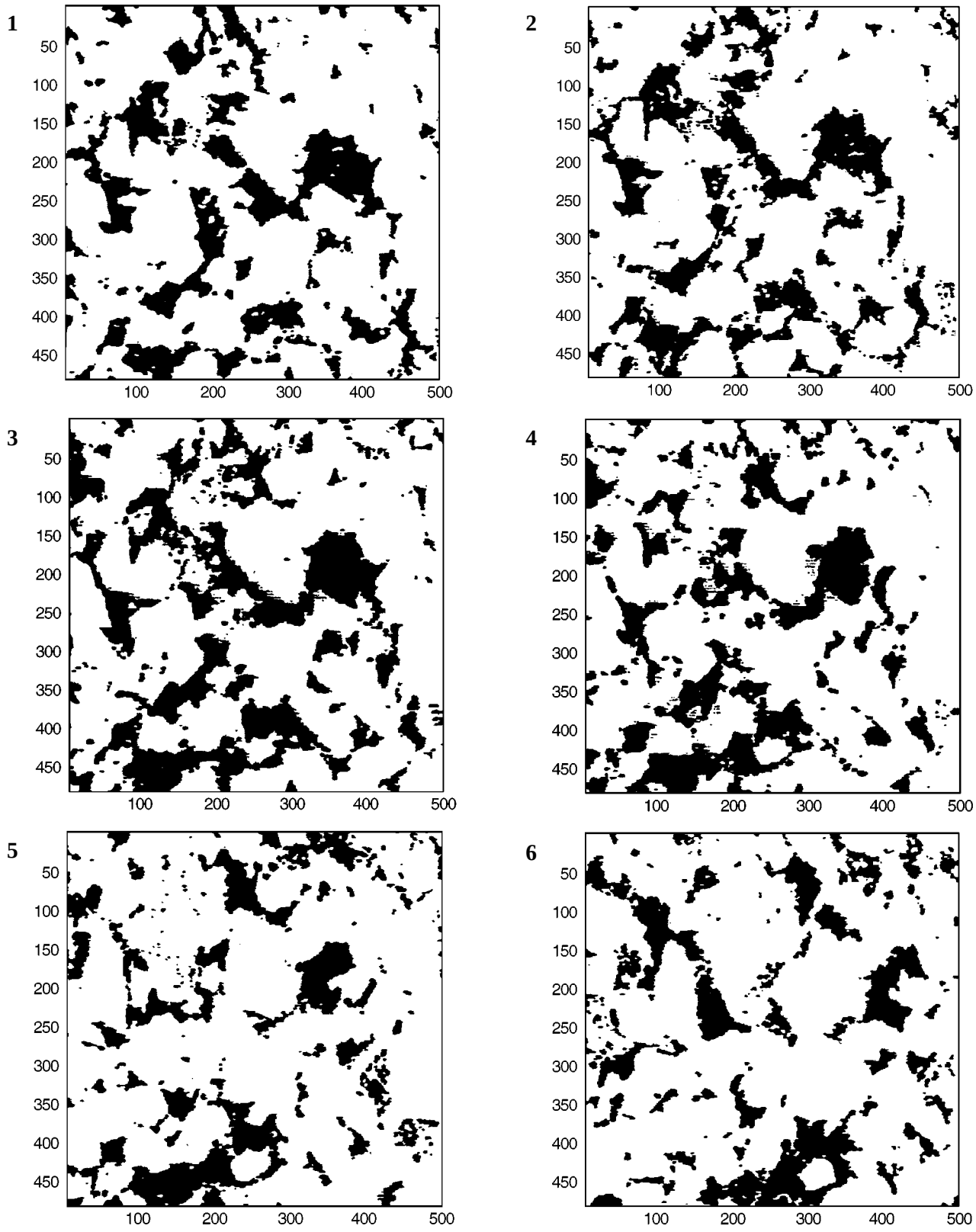

Figure 1

Visualization of the six binary images of the serial cross-sections in set (3A1).
A pixel is equal to 2.04 μm.

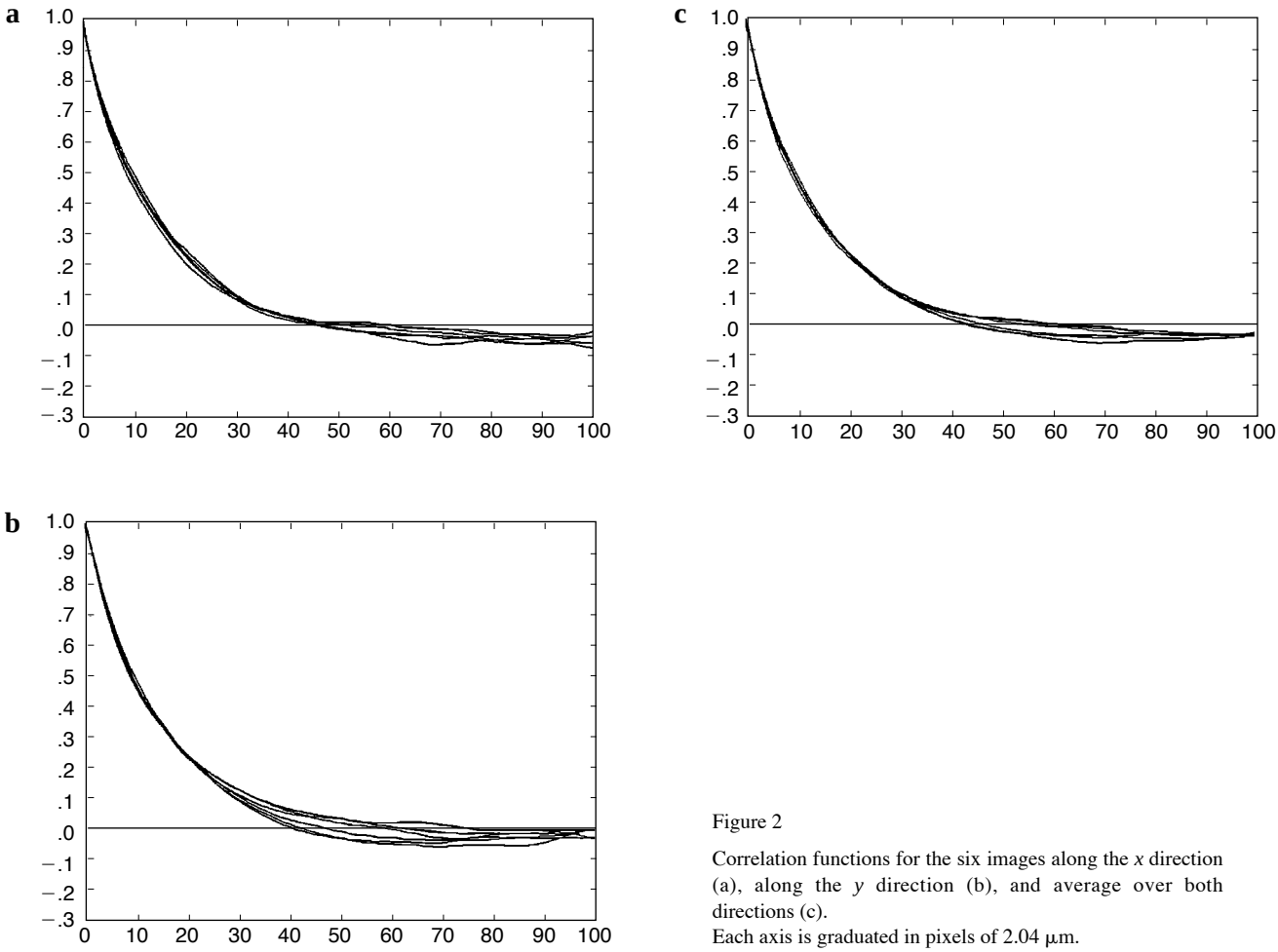

Figure 2

Correlation functions for the six images along the *x* direction (a), along the *y* direction (b), and average over both directions (c).
Each axis is graduated in pixels of 2.04 μm.

TABLE 1

Porosity of the images (ε) and of the half-images (ε_1, ε_2) for the sample (3A1)

Section	ε	ε_1	ε_2	$\varepsilon_1 - \varepsilon_2$
1	0.223	0.262	0.184	0.078
2	0.229	0.279	0.179	0.100
3	0.273	0.329	0.217	0.112
4	0.240	0.301	0.179	0.122
5	0.203	0.235	0.171	0.064
6	0.215	0.205	0.225	− 0.020
Average	0.231	0.268	0.193	0.075
Standard deviation	0.025	0.046	0.023	
Plug	0.210			

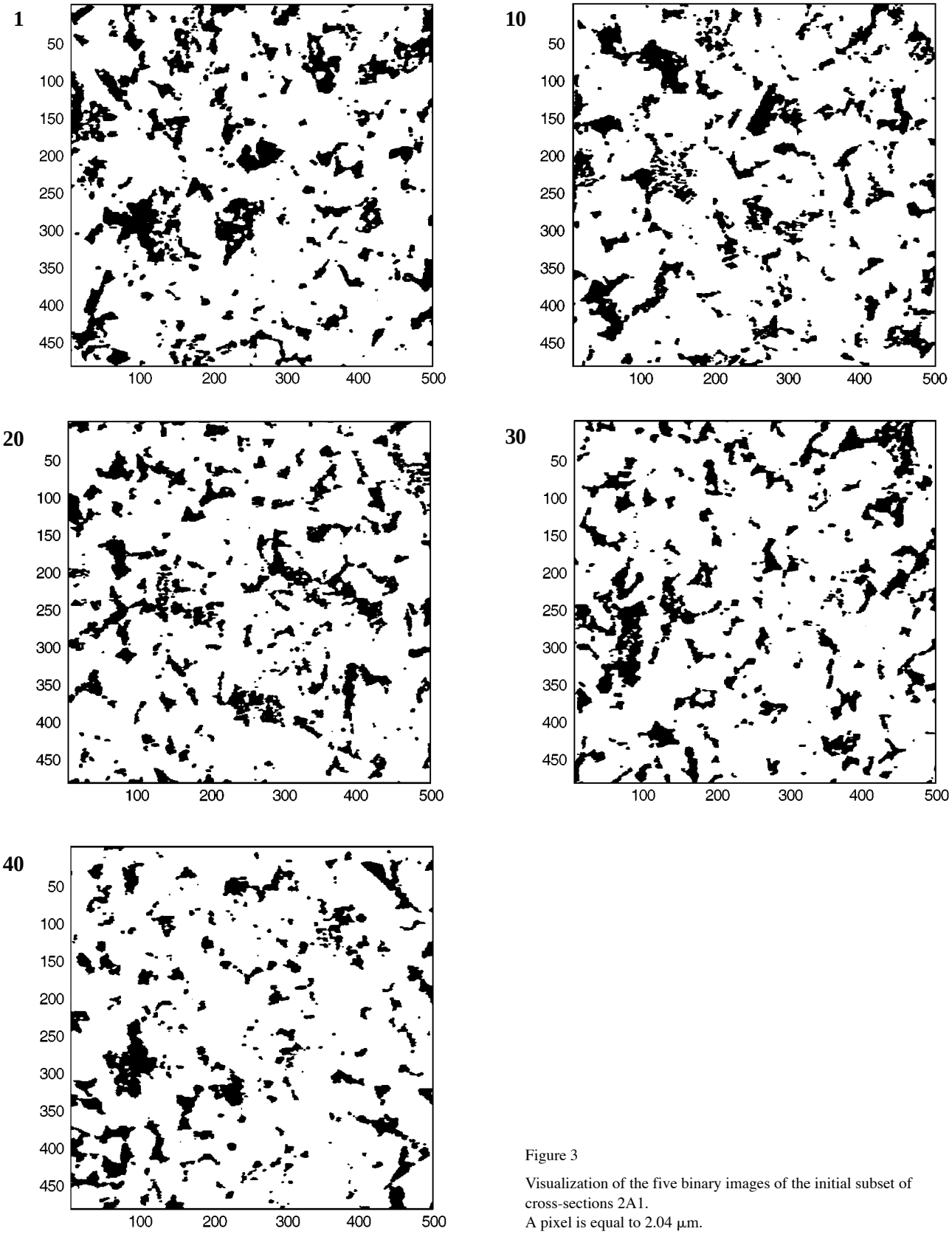

Figure 3

Visualization of the five binary images of the initial subset of cross-sections 2A1.
A pixel is equal to 2.04 μm.

TABLE 2

Porosity of the images (ε) and of the half-images (ε_1, ε_2) for the sample (2A1). The lines corresponding to the initial subset of five images are printed boldface, and their statistics are given separately

Section	ε	ε_1	ε_2	$\varepsilon_1 - \varepsilon_2$
1	**0.188**	**0.222**	**0.154**	**0.068**
2	0.164	0.188	0.139	0.048
3	0.167	0.188	0.144	0.044
4	0.169	0.190	0.148	0.042
5	0.201	0.210	0.193	0.017
6	0.183	0.197	0.170	0.027
7	0.177	0.193	0.161	0.032
8	0.171	0.191	0.151	0.041
9	0.173	0.188	0.158	0.030
10	**0.166**	**0.177**	**0.156**	**0.020**
11	0.171	0.184	0.157	0.027
12	0.157	0.167	0.147	0.020
13	0.187	0.209	0.166	0.043
14	0.191	0.215	0.168	0.047
15	0.181	0.204	0.158	0.046
16	0.163	0.171	0.155	0.016
17	0.162	0.162	0.162	- 0.000
18	0.155	0.158	0.152	0.005
19	0.131	0.143	0.118	0.025
20	**0.160**	**0.159**	**0.162**	**- 0.003**
21	0.131	0.127	0.135	- 0.008
22	0.132	0.128	0.136	- 0.008
23	0.150	0.144	0.157	- 0.013
24	0.180	0.178	0.182	- 0.004
25	0.167	0.165	0.169	- 0.003
26	0.166	0.159	0.173	- 0.014
27	0.170	0.169	0.172	- 0.002
28	0.162	0.149	0.175	- 0.026
29	0.173	0.183	0.164	0.019
30	**0.171**	**0.184**	**0.159**	**0.026**
31	0.156	0.165	0.147	0.019
32	0.150	0.150	0.149	0.001
33	0.161	0.157	0.165	- 0.008
34	0.170	0.171	0.169	0.001
35	0.151	0.151	0.151	- 0.000
36	0.158	0.150	0.167	- 0.017
37	0.157	0.153	0.161	- 0.008
38	0.153	0.168	0.137	0.031
39	0.153	0.173	0.133	0.040
40	**0.139**	**0.161**	**0.117**	**0.044**
41	0.155	0.184	0.125	0.059
42	0.151	0.183	0.119	0.064
43	0.151	0.185	0.118	0.066
44	0.165	0.200	0.130	0.070
45	0.171	0.206	0.136	0.070
Average	0.164	0.175	0.153	0.022
(subset)	**0.165**	**0.181**	**0.150**	**0.031**
Standard deviation	0.015	0.022	0.018	
(subset)	**0.016**	**0.023**	**0.016**	

The statistics of the subset are typical of the complete sample.

The correlation function was measured on all of the 45 images, along the *x*- and *y*-axes. Again, it was found to be almost identical in both directions and for all the images. In particular, the curves for the images of the subset (Figure 4) are representative of the complete sample. Therefore, we used the average porosity ε and the average *x*- or *y*-correlation function evaluated on the subset as input data for the reconstruction. Again, the correlation function is not affected by the inhomogeneity of the porosity.

So far, the three-dimensional aspect of the experimental data has not been taken into account. This is done in Figure 5-a, where the correlation function R_z along the direction normal to the serial sections is compared to the correlations R_x and R_y within their planes for the data-set (3A1). R_z shows kinks which are not typical of the usual correlations for geological materials. In addition, the initial decrease of the correlation is much steeper for R_z than for R_x or R_y.

It has already been mentioned that the successive frames are not perfectly aligned in the *z* direction, but are slightly shifted with respect to one another. Despite the use of a frame of reference for edge detection, some slight shift appears to be inevitable. We attempted to compensate this artifact by realigning the 45 frames. This was done by maximising the pointwise covariance of the successive frames *k* and $k + 1$

$$\sum_i \sum_j Z_k(i, j)\, Z_{k+1}(i+u,\ j+v) \qquad (3)$$

and the result was in good agreement (within about 1 pixel) with the subjective guess resulting from a visual superposition of the successive images. The dimension of the largest parallelepiped entirely covered by the 45 frames after realignment is $466 \times 472 \times 45$ (vs. $500 \times 482 \times 45$ for the raw data). The correlation function R_z evaluated on this modified data set is displayed on Figure 5b. It appears that this procedure filters out the kinks of the curve on Figure 5a, and that the short-range correlations are now identical along the three axes. However, the correlation R_z is definitely stronger than R_x or R_y for intermediate distances in a 10 to 100 μm range. This can be quantified by the correlation length $\mathcal{L}$, defined as the integral of the correlation function,

$$\mathcal{L} = \int_0^\infty R(u)du \qquad (4)$$

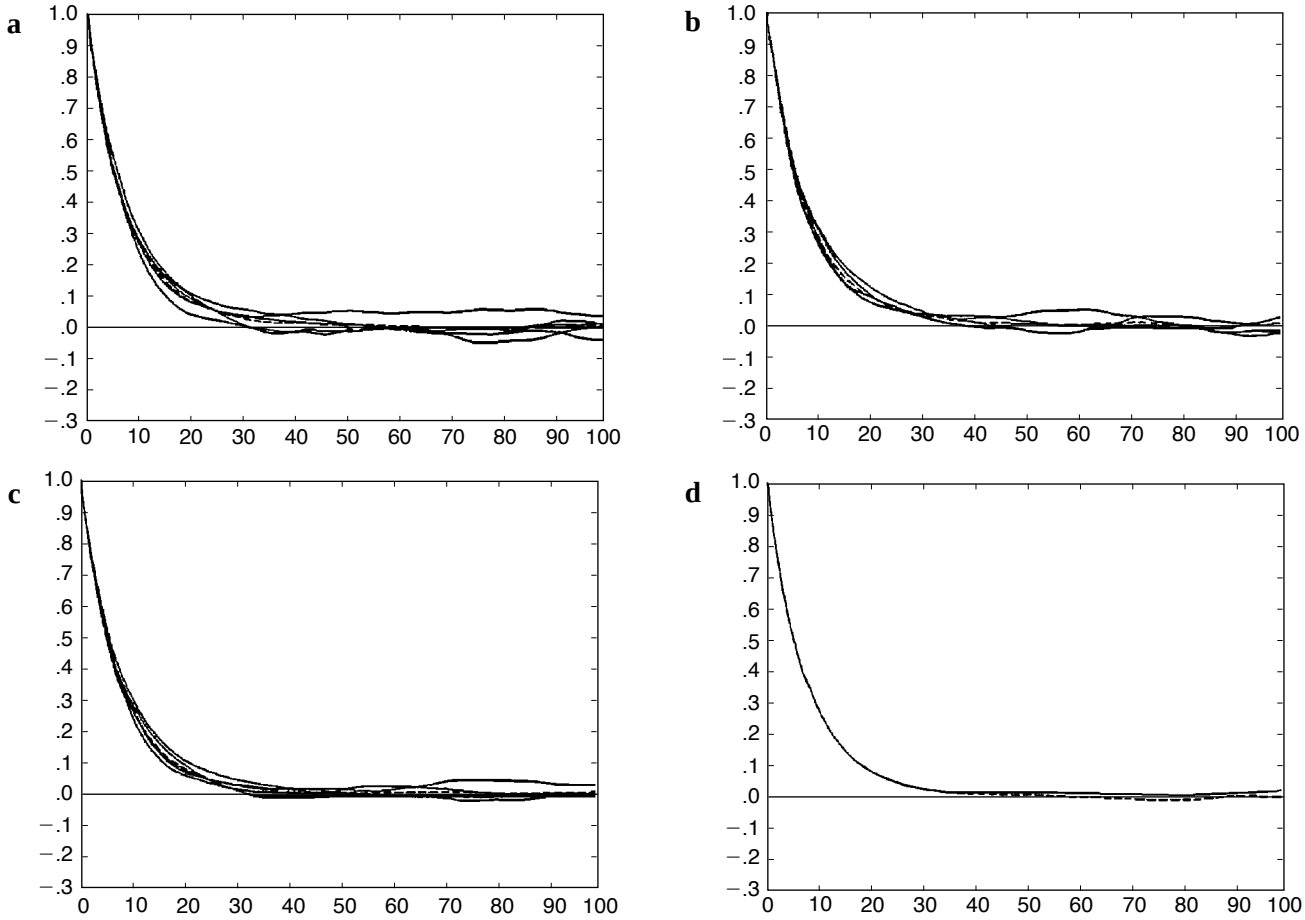

Figure 4

Correlation functions for the five images of the subset (2A1) along the *x* direction (a), along the *y* direction (b), and averaged over both directions (c).
The average curves along the *x* direction for the subset and the complete sample are compared in (d). The axes are graduated in pixels of 2.04 μm.

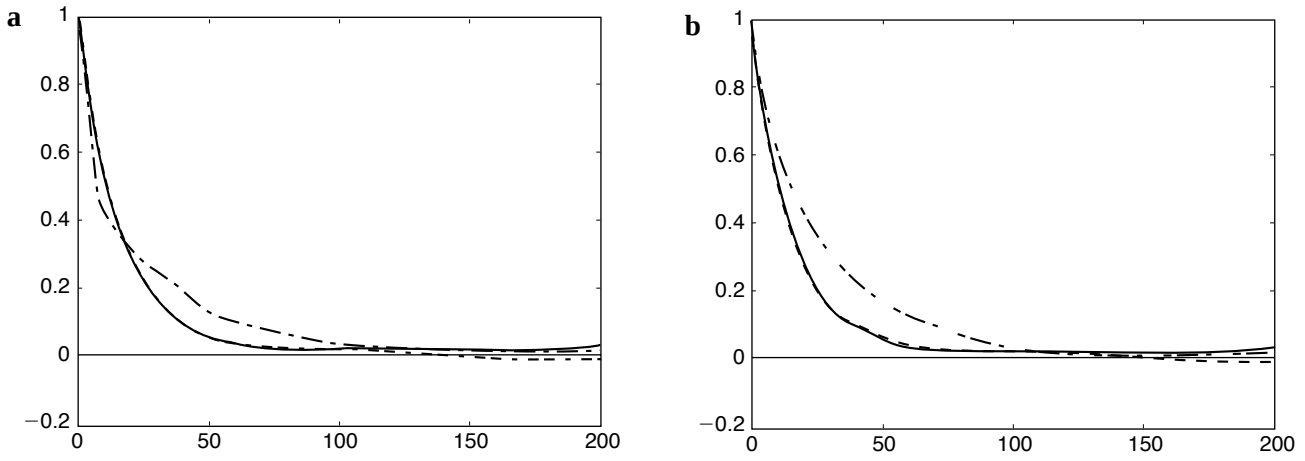

Figure 5

Correlation functions for set (2A1) along the *x*-(solid line), *y*-(dash line), and *z*-direction (dot-dash), before (a) and after (b) realignment of the successive sections.
Distances are measured in microns.

This length, evaluated along the three axes before and after the realignment, is given in Table 3. Part of the difference between $\mathcal{L}_z$ and $\mathcal{L}_x$ or $\mathcal{L}_y$ might result from the realignment procedure, though $\mathcal{L}_z$ is larger than $\mathcal{L}_x$ or $\mathcal{L}_y$ even in the raw data. If real, this difference suggests that the material is anisotropic, for example with a slight stratification parallel to the cross-sections. Since its existence is not firmly established, this anisotropy is ignored in the rest of this work. Only the correlations along directions within the serial sections are retained.

TABLE 3

Correlation length for data-set (2A1) in microns

	Raw data	After realignement
$\mathcal{L}_x$	17.8	17.8
$\mathcal{L}_y$	17.5	17.5
$\mathcal{L}_z$	20.6	26.7

2 GENERATION OF RANDOM DISCRETE VARIABLES WITH GIVEN AVERAGE AND CORRELATION FUNCTION

Let us now briefly sketch the reconstruction of three-dimensional random media which is fully described in Adler *et al.* (1990). We want to generate a three-dimensional random porous medium with a given porosity ε and a given correlation function; the medium is homogeneous and virtually isotropic. It should be emphasized that the correlation function of isotropic media depends only on the norm u of the vector $\boldsymbol{u}$ (see R.J. Adler, 1981).

Similarly, we want to generate a random function of space $Z(\boldsymbol{x})$ which is equal to 0 in the solid phase and to 1 in the liquid phase. $Z(\boldsymbol{x})$ has to reproduce the two average properties (2a) and (2b) accurately (Quiblier, 1984). It should be emphasized that the point of view is quite different here; ε is a given positive number < 1; $R_z(u)$ is a given function of u which satisfies the general properties of a correlation (see Adler, 1981) but is otherwise arbitrary.

For practical purposes only, the porous medium is constructed in a discrete manner. It is considered to be composed of N_c^3 small cubes, each of the same size a. These elementary cubes are filled either with liquid, or with solid. Examples of such porous media have already been given elsewhere (Lemaître and Adler, 1990; Adler, 1992). Hence the position vector $\boldsymbol{x}$ and the translation vector $\boldsymbol{u}$ will only take discrete values; the corresponding trios of integers are denoted by

$$\boldsymbol{x}' = \boldsymbol{x}/a = (i,\ j,\ k) \tag{5a}$$

$$\boldsymbol{u}' = \boldsymbol{u}/a = (r,\ s,\ t) \tag{5b}$$

An additional condition is imposed by the fact that the sample of the generated porous medium has a finite size equal to aN_c. This is equivalent to covering of the whole porous medium with an infinite number of identical unit cells. Since the medium is assumed to be uniformly correlated, the random field $Z(\boldsymbol{x})$ has to satisfy the relation

$$\varepsilon = < Z(\boldsymbol{x}) > \tag{6a}$$

$$R_z(\boldsymbol{u}) = R_z(u) = < (Z(\boldsymbol{x}) - \varepsilon) (Z(\boldsymbol{x}_t) - \varepsilon) >/(\varepsilon - \varepsilon^2) \tag{6b}$$

where the translated vector $\boldsymbol{x}_t$ is defined mod (aN_c) for each of its components:

$$\boldsymbol{x}_t = \boldsymbol{x} + \boldsymbol{u} \pmod{aN_c} \tag{7a}$$

This equality means that, for instance,

$$i_t = i + r \pmod{N_c} \tag{7b}$$

Because of this spatial periodicity, all the physical quantities are independent of the choice of origin and faces of unit cells.

There are several methods to generate discrete random variables which satisfy (6a) and (6b). Here we adapt to isotropic media an algorithm due to Quiblier (1984), for general three-dimensional porous media. This algorithm is itself an extension of the two-dimensional scheme devised by Joshi (1974).

For the sake of clarity, we briefly present this algorithm in the present section and recall the major properties of the corresponding random functions. It can be shown that a random and discrete field $Z(\boldsymbol{x})$ can be constructed from a Gaussian field $X(\boldsymbol{x})$ when the latter is successively passed through a linear and a nonlinear filter. Let us summarize the influence of these filters and relate their properties to the statistical properties of the resulting fields. A detailed presentation can be found in Adler *et al.* (1990).

Consider, first, the initial random field $X(i, j, k)$; the random variables $X(i, j, k)$ are assumed to be normally distributed with a mean equal to 0 and a variance equal to 1; these variables are independent.

A linear operator can be defined by an array of coefficients $\bar{a}(\boldsymbol{u}')$ where $\boldsymbol{u}'$ belongs to a finite cube $[0, Lc]^3$ in Z^3. Outside this cube, it is equal to 0. A new random field $Y(\boldsymbol{x}')$ can be expressed as a linear combination of the random variables $X(\boldsymbol{x}')$:

$$Y(\boldsymbol{x}') = \sum_{\boldsymbol{u}' \in [0, L_c]^3} \bar{a}(\boldsymbol{u}') \cdot X(\boldsymbol{x}'_t) \tag{8}$$

where the translated vector $\boldsymbol{x}'_t$ is defined mod N_c for each of its components.

The definition (8) is identical to the definition used by Joshi (1974) and Quiblier (1984), except for the periodic character introduced by the condition mod N_c. Without any further requirements on the coefficients $\bar{a}(\boldsymbol{u}')$ of the linear filter, it can be shown that the random variables $Y(\boldsymbol{x}')$ are standard Gaussian if $N_c > 2L_c$. Let us further assume that the variance of $Y(\boldsymbol{x}')$ is equal to 1,

$$E\{Y^2(\boldsymbol{x})\} = 1 \tag{9}$$

Hence the random variables $Y(\boldsymbol{x}')$ have a standard normal distribution, although they are no longer statistically independent. Their correlation function $R_y(u)$ is easily seen to be

$$R_y(u) = \sum_{r, s, t \in [0, L_c]} \bar{a}_{u_1, u_2, u_3} \cdot \bar{a}_{u_1 + r, u_2 + s, u_3 + t} \tag{10}$$

where $(u_1 + r)$, $(u_2 + s)$, $(u_3 + t)$ are determined mod N_c and $u = (u_1^2 + u_2^2 + u_2^3)^{1/2}$. The random field $Y(\boldsymbol{x}')$ is correlated, but still not satisfactory since it takes its values in R, while the porous medium has to be represented by a discrete-valued field $Z(\boldsymbol{x}')$ (cf. Joshi, 1974). In order to extract such a field from $Y(\boldsymbol{x}')$, one applies a nonlinear filter G, i.e. the random variable Z is a deterministic function of Y,

$$Z = G(Y) \tag{11}$$

When G is known, the statistical properties of the random field Z can be derived from those of Y. For the sake of completeness, this derivation, which can be found in Joshi (1974), is briefly repeated here.

Since the random variable $Y(\boldsymbol{x}')$ has a standard normal distribution (i.e. with a zero mean and a variance equal to 1), its distribution function $P(y)$ is given by:

$$P(y) = (2\pi)^{-1/2} \int_{-\infty}^{y} e^{(-y^2/2)} dy \tag{12}$$

The deterministic function G is defined by the following condition: when the random variable Y is equal to y, Z takes the value z

$$z = 1 \quad \text{if} \quad P(y) \leqslant \varepsilon \tag{13a}$$

$$z = 0 \quad \text{otherwise} \tag{13b}$$

It is, thus, fairly obvious that the average value of $Z(\boldsymbol{x}')$ is equal to ε, and its variance to $\varepsilon - \varepsilon^2$.

The most difficult point is the determination of the correlation function $R_z(u)$ of $Z(\boldsymbol{x}')$ as a function of $R_y(u)$. One can start from the fact that the random variable $(Y(\boldsymbol{x}'), Y(\boldsymbol{x}' + \boldsymbol{u}'))$ is a bivariate Gaussian whose probability density is known (see e.g. R.J. Adler, 1981); this density can be expanded in terms of Hermite polynomials. After some tedious manipulations using classical identities (Gradshteyn and Ryshik, 1965), $R_z(u)$ can be expressed as a series in terms of $R_y(u)$

$$R_y(u) = \sum_{m=0}^{\infty} C_m^2 \cdot R_y^m \tag{14}$$

where the coefficients C_m are given by

$$C_m = (2\pi m!)^{-1/2} \int_{-\infty}^{\infty} c(y) e^{-y^2/2} H_m(y) dy \tag{15a}$$

together with

$$c(y) = (\varepsilon - 1) / [\varepsilon (1 - \varepsilon)]^{1/2} \quad \text{if} \quad P(y) \leqslant \varepsilon \tag{15b}$$

$$c(y) = \varepsilon / [\varepsilon (1 - \varepsilon)]^{1/2} \quad \text{if} \quad P(y) > \varepsilon \tag{15c}$$

and

$$H_m(y) = (-1)^m e^{y^2/2} \frac{d^m}{dy^m} e^{-y^2/2} \tag{15d}$$

3 SIMULATION OF REAL POROUS MEDIA

When the aim is to simulate a given porous medium, the first problem is the determination of the correlation function $R_y(u)$ and of the set of coefficients $\bar{a}$: this is what we shall call the inverse problem. Once these coefficients have been calculated, porous media can be simulated and their general properties critically examined.

Let us first briefly sketch a direct method to address the inverse problem. When the porosity is given, the correlation function $R_y(u)$ is easily derived from $R_z(u)$; this simply corresponds to the numerical inversion of (14) and (15) by any standard method such as a Newton iterative scheme.

When $R_y(u)$ is known, one has to determine the coefficients $\bar{a}$ by solving the set of quadratic equations (10). This step can only be performed numerically by using standard optimization routines; it should be noted that the solution is not unique and that it was sometimes difficult to determine $\bar{a}$. Again, further details on the inverse problem can be found in Adler *et al.* (1990).

Once the coefficients $\bar{a}$ are obtained, arbitrary samples of porous media can be reconstructed. One starts from an arbitrary seed and then generates a set of independent Gaussian variables $X(i, j, k)$; then, this set is successively passed through the linear filter (8) and the nonlinear filter (11), (12) and (13).

From the numerical point of view, the most demanding step of the previous procedure is the solution of the set of nonlinear equations (10) for the coefficients $\bar{a}$. For this reason, an alternative algorithm was used in this study, in which the $\bar{a}$'s are not derived explicitly. Once the $R_y(u)$ function has been evaluated as stated above, the $Y(\boldsymbol{x}')$ field is deduced from the X field by the inverse Fourier transform

$$Y(\boldsymbol{x}') = N_c^{3/2} \sum_{\boldsymbol{m}} (\hat{R}_{Y\boldsymbol{m}})^{1/2} \hat{X}_{\boldsymbol{m}} e^{-2i\pi \boldsymbol{k_m} \cdot \boldsymbol{x}'} \qquad (16)$$

where $\hat{R}_{Y\boldsymbol{m}}$ and $\hat{X}_{\boldsymbol{m}}$ are the coefficients of the discrete Fourier transform of R_y and X respectively. The nonlinear filter G is then applied to Y as in the former case. Further details on this new method of solution can be found in Adler (1992). In particular, it is shown there that equation (16) yields a Y field which is indeed a linear combination of the X variables similar to (8).

It should be noted that when Gaussian variables are used, all the moments of the phase functions are determined when the two first moments (i.e. porosity and correlation function) are given. Hence, one may wonder whether the moments of order n

$$R(\boldsymbol{u}_1, \boldsymbol{u}_2, \ldots, \boldsymbol{u}_{n-1}) = (\varepsilon - \varepsilon^2)^{-n/2} \left\langle (Z(\boldsymbol{x}) - \varepsilon) \prod_{\alpha=1}^{n-1} (Z(\boldsymbol{x} + \boldsymbol{u}_\alpha) - \varepsilon) \right\rangle \qquad (17)$$

are the same in the real and in the reconstructed materials. Yao *et al.* (1992) recently showed that this is indeed the case on three-dimensional samples at least up to the fourth order moment of the phase function. This is a very important result which gives additional confidence in the reconstruction method.

4 RESULTS AND DISCUSSION

Since the original material has been shown to be isotropic, with no significant difference between the correlation functions of the various cross-sections, we made use of the average R_Z function (i.e. the average of the curves of Figure 2a, 2b or 4a, 4b) for the reconstruction. However, in view of the dispersion of the porosities in the various sections, the global porosity $\varepsilon = 0.210$ of the plug for (3A1), and the average over the 45 sections $\varepsilon = 0.164$ for (2A1) were used as input data.

For the sample (3A1), the correlation function was discretized over 10 points, including the origin $R_z(0) = 1$, with a 6 pixels ≈ 12.2 μm spacing, which is the linear dimension of the elementary cubes of the reconstructed samples.

Figure 6 presents a three-dimensional visualization of a reconstructed medium with $N_c = 64$, which corresponds to $(783\ \mu m)^3$ in physical dimensions. Its porosity is 0.209. Only the pore space is displayed, within a cubic wireframe which corresponds to the boundaries of the unit cell of the infinite periodic medium.

Samples of this size are somewhat too large to allow an extensive study of their transport properties. Recall that a sample with $N_c = 64$ contains 262 144 elementary cubes and that the determination of the permeability, for example, involves the solution of the Stokes equation for the velocity and pressure fields, i.e. four unknowns at each liquid node. For an average porosity of 0.21, 220 000 (resp. 1 760 000) unknowns have to be determined when the elementary cube is discretized in 1 (resp. $2^3 = 8$) mesh points. Therefore, smaller samples have also been reconstructed with $N_c = 33$, which corresponds to $(404\ \mu m)^3$ in physical dimensions. Note that this dimension is still much larger than the correlation length (4) of the medium ($\mathcal{L} \approx 27$ mm).

For the data set (2A1),the correlation function was discretized over 17 points, including the origin, with a 5 pixels 10.2 μm spacing. Five samples with $N_c = 33$, i.e. $(337\ \mu m)^3$, were reconstructed. Their porosities ranged from 0.135 to 0.227, with an average 0.180. Smaller ($N_c = 20$) or larger ($N_c = 55$) samples were

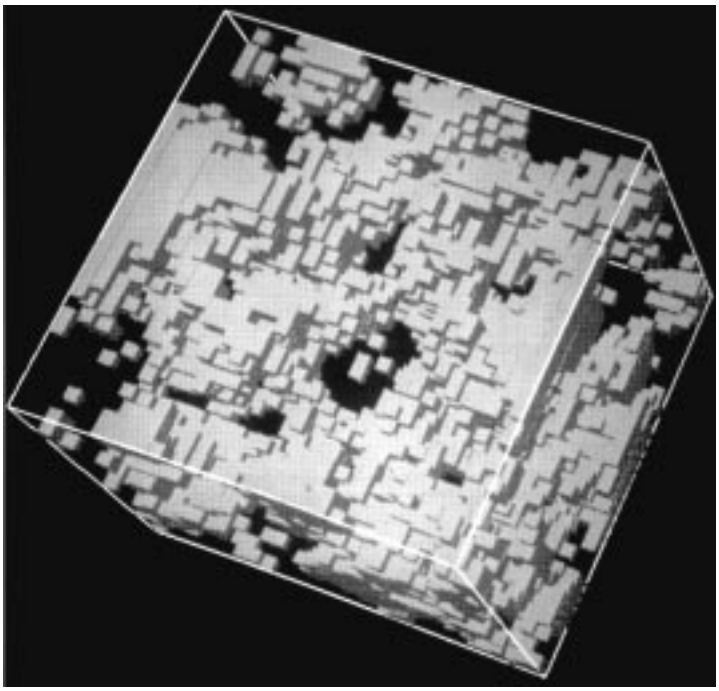

Figure 6

Pore space of a reconstructed sample for (3A1) with $N_c = 64$ (783 μm)^3.
The porosity is 0.209.

also reconstructed for specific studies (Taylor dispersion and mercury porosimetry). They are presented below when they are used.

5 TRANSPORT PROCESSES: METHODS OF SOLUTION

The permeability, the formation factor and the dispersivity of these reconstructed media can be calculated numerically by solving the local equations with the appropriate boundary conditions (Adler, 1992). The flow problem is solved here using an improved version of the method proposed by Lemaître and Adler (1990). In order to cope with the continuity equation, the so-called artificial compressibility method was applied with a staggered marker-and-cell (MAC) mesh (Peyret and Taylor, 1985). In essence, the problem is replaced by an unsteady compressible one which is assumed to converge towards the steady incompressible situation of interest. Additional details can be found in Adler *et al.* (1990). Note that our formulation is consistent; for instance, if two solid cubes have only one edge in common, no fluid can flow through this edge. The diffusion problem is solved via a second-order finite-difference formulation (Thovert *et al.*, 1990). A conjugate-gradient method turned out to be very effective for the problem at hand, primarily because it is better suited to vectorial programming than implicit relaxation schemes. The computations were run on various vectorial computers, with an acceleration factor ranging from 4 to 6 with respect to an optimized scalar execution. The dispersivity can be calculated by solving the convection-diffusion equation or through Monte Carlo simulation of the displacement of a large number of particles inside the fluid (Salles *et al.*, 1993 a, b).

6 TRANSPORT PROCESSES: RESULTS AND DISCUSSION

The computed values of the permeabilities and formation factors for the various reconstructed samples are listed in Table 4 (for 3A1) and Table 5 (for 2A1). For both transport processes and for every sample the

complete macroscopic tensor $\boldsymbol{K}$ (permeability) or $\overline{\sigma}$ (conductivity) was determined by computing the fluxes $\overline{\boldsymbol{v}}$ or $\overline{\boldsymbol{q}}$ with a unit driving gradient $\overline{\nabla p}$ or $\overline{\nabla T}$ set along the *x*-, *y*- and *z*-axes successively. Then a scalar parameter K or $\overline{\sigma}$ was obtained by taking the average of the diagonal terms of the tensors

$$K = (K_{11} + K_{22} + K_{33})/3 \qquad (18a)$$

$$\overline{\sigma} = (\overline{\sigma}_{11} + \overline{\sigma}_{22} + \overline{\sigma}_{33})/3 \qquad (18b)$$

$$F = 1/\overline{\sigma} \qquad (18c)$$

The porosity ε and the open porosity ε_0 of the reconstructed media are also reported in the tables.

The permeability and conductivity are significantly larger for the sample (3A1) than for (2A1). This results from at least two facts. First, (3A1) has a higher porosity (0.21) than (2A1) (0.164). Second, (3A1) shows correlations over larger distances. This can be quantified by the correlation length $\mathcal{L}$, defined as the integral of the correlation function (4), which is a characteristic length scale of the microstructure. It is equal to 27 μm in (3A1), and only to 18 μm in (2A1). This difference suggests that the quartz grains of the solid matrices might be somewhat larger in (3A1). The ratio $K/(\overline{\sigma}\,\mathcal{L}^2)$, which eliminates part of the influence of the scale of the microstructure and in some respects of the porosity and tortuosity, is comparable for (3A1) and (2A1) (0.033 and 0.054 respectively).

The average computed values of the permeability and formation factor are compared in Figure 7 to previous experimental and numerical data relative to Fontainebleau sandstones (Adler *et al.*, 1990). Comparable results are obtained for (3A1), which is not surprising since the Fontainebleau sandstones have also a correlation length $\mathcal{L}$ of roughly 25 microns in a porosity range around 0.20. The sample (2A1) yields a lower permeability and a higher formation factor, due in part to its finer microstructure.

TABLE 4

Permeability and conductivity computed for the reconstructed samples for set (3A1)

Sample	ε	ε_0	K (mD)	$\overline{\sigma}$	F
1	0.208	0.194	169	0.0107	93.5
2	0.211	0.183	217	0.0128	78.1
3	0.247	0.242	1 086	0.0348	28.7
4	0.264	0.255	831	0.0376	26.6
5	0.181	0.165	141	0.0090	111.1
Average	0.222	0.208	489	0.0210	67.6

TABLE 5

Permeability and conductivity computed for the reconstructed samples for set (2A1)

Sample	ε	ε_0	K (mD)	$\overline{\sigma}$	F
1	0.170	0.132	7.6	0.0009	1045
2	0.170	0.141	30.1	0.0034	298
3	0.200	0.182	117	0.0107	946
4	0.227	0.210	134	0.0117	85.8
5	0.135	0	0	0	-
Average	0.180	0.133	57.7	0.0034	294

6.1 Experimental permeability-porosity correlation

The results found concerning the values of the permeability versus porosity are summarized here.

- From two plugs of Vosges sandstone cut in the block in the vicinity of the long cores, the results are:

$$\text{plug 3A1} \quad \varepsilon = 0.22 \quad K = 92 \text{ mD}$$

$$\text{plug 2A1} \quad \varepsilon = 0.236 \quad K = 145 \text{ mD}$$

in this case, K is the air permeability.

- The long core 3B (Length = 35 cm, with a square cross-section having 4 cm in side) has been CT-scanned resulting:
  – in a density profile expressed in Hounsfield units (Fig. 8);
  – in a porosity profile: along the whole core and along 11 slices every 3 cm with 8 mm in thickness in the center part of the core, showing a good homogeneity:

$$0.196 < \varepsilon < 0.204$$

On the other hand, the absolute permeability with brine has been measured and again a good macroscopic homogeneity has been found:

$K_a = 73$ mD in the 35 cm core;
$K_a = 72$ mD in the central part of the core.

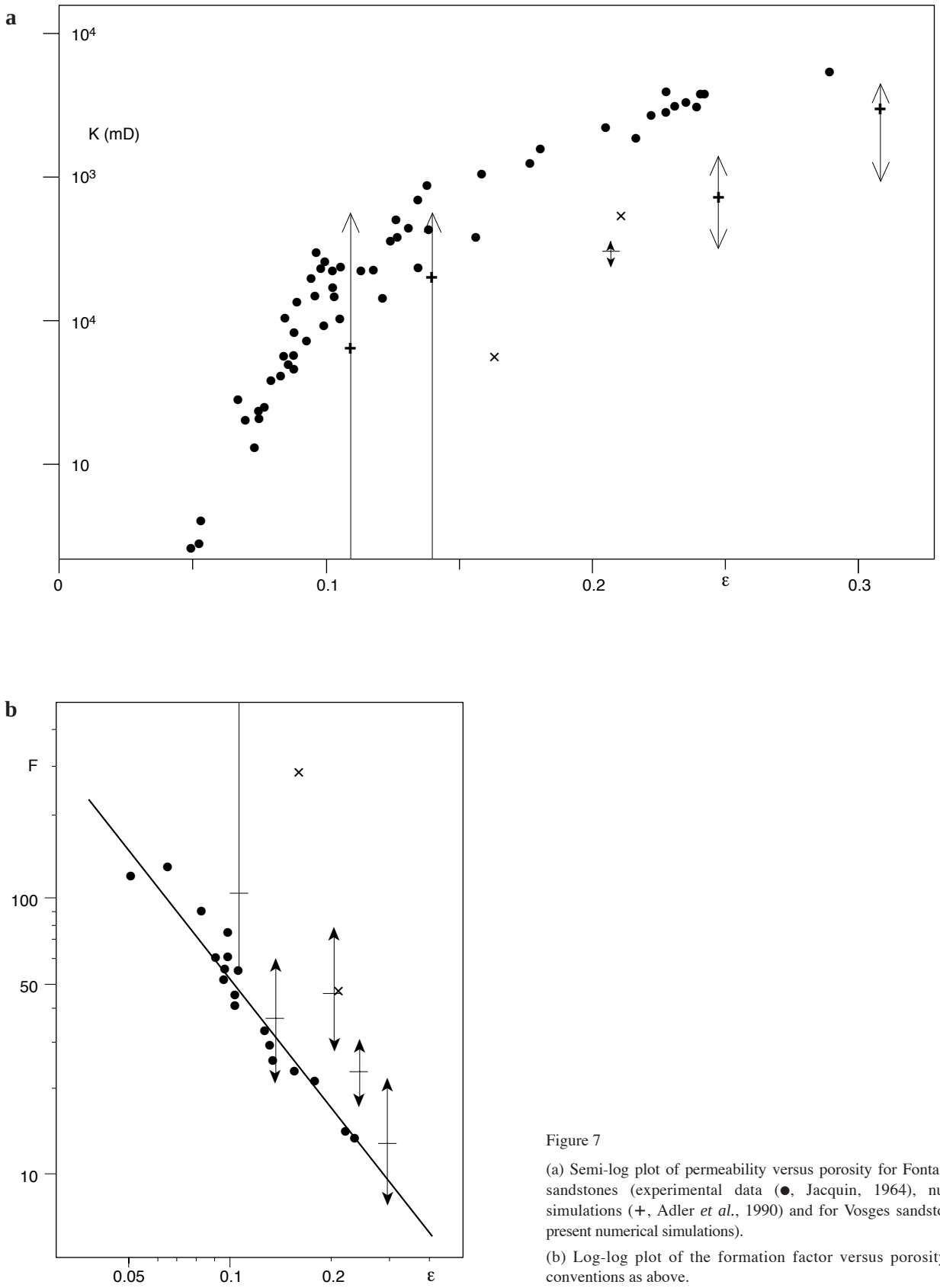

Figure 7

(a) Semi-log plot of permeability versus porosity for Fontainebleau sandstones (experimental data (●, Jacquin, 1964), numerical simulations (+, Adler *et al.*, 1990) and for Vosges sandstones (×, present numerical simulations).

(b) Log-log plot of the formation factor versus porosity. Same conventions as above.

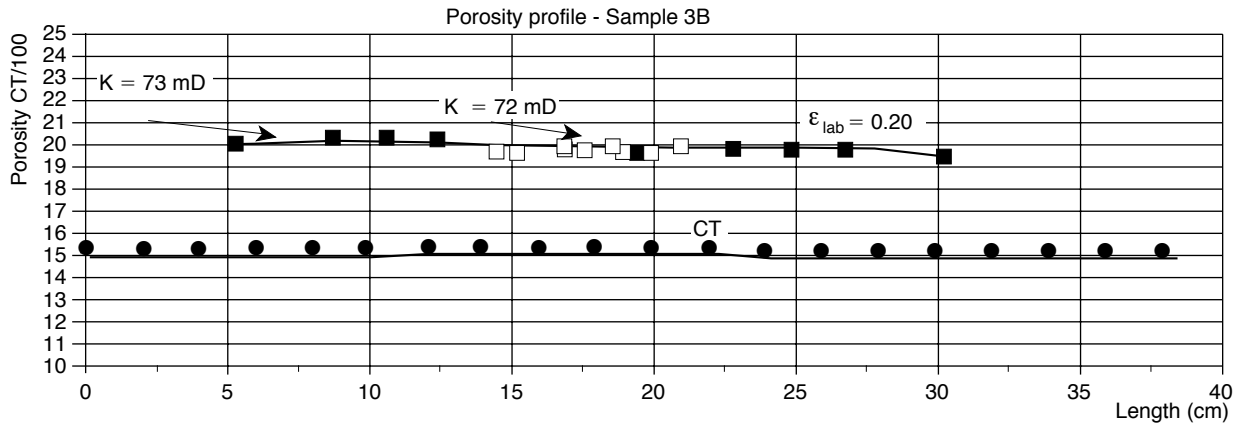

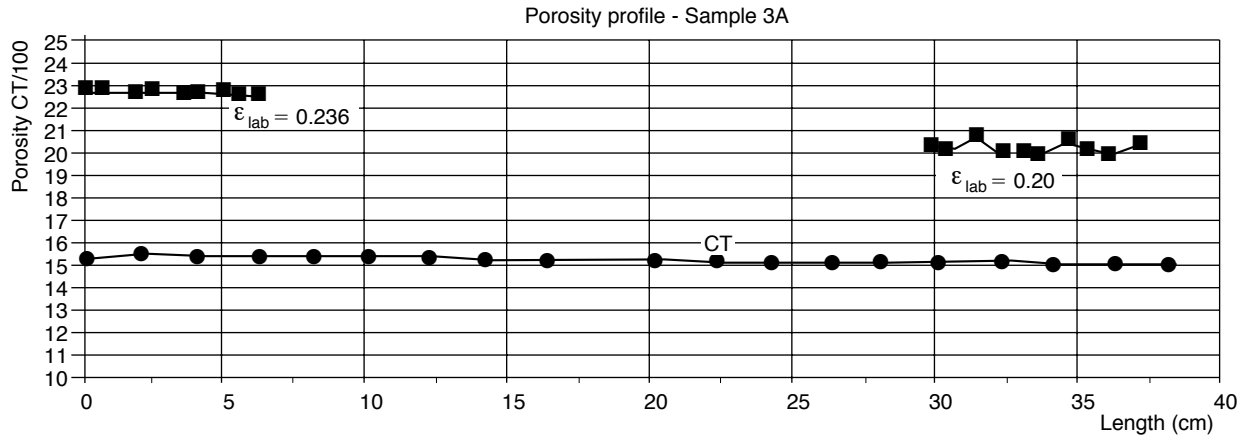

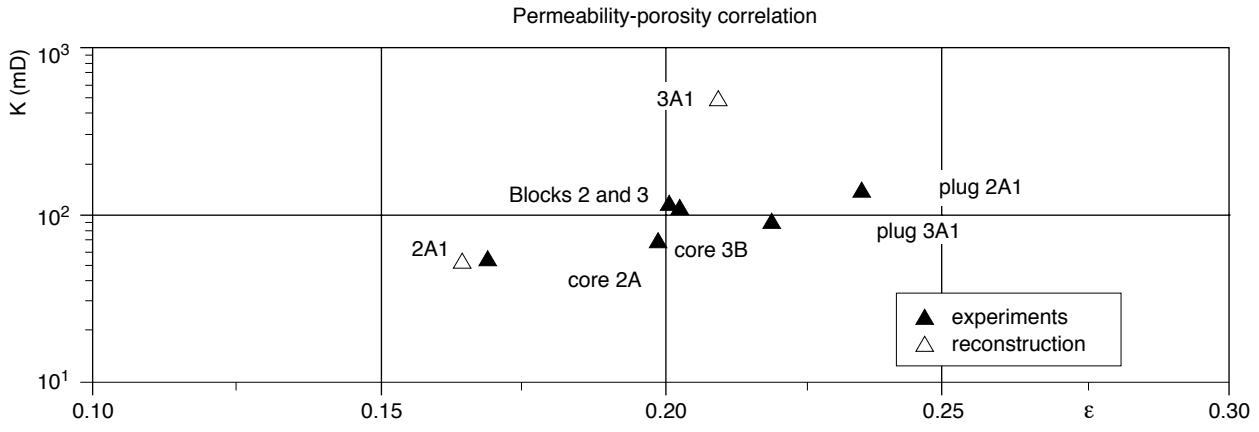

Figure 8

Plot of experimental porosity and CT profiles for Vosges sandstones.
Semi-log plot of permeability versus porosity: comparison between numerical simulation and measured values.

- The long core 2A, exhibits a mean porosity value of $\varepsilon = 0.17$ with a permeability to the brine used, $K = 56$ mD.
- The long core A3 has been cut into several parts. The measurements on only two parts of this sample (see Figure 8) show porosity values around 0.2 for one part and 0.236 for the other one, corresponding to the CT profile found earlier.
- Measurements performed with air on the small samples cored in the top part of the blocks for the mercury intrusion study give the following results:
  - Block 2 $\varepsilon = 0.204$ $K_a = 111$ mD
  - Block 3 $\varepsilon = 0.202$ $K_a = 118$ mD

The results of these measurements are displayed in Figure 8, together with the results found after the reconstruction. It can be seen from the experimental results that the porosity displays values between 0.17 and 0.236. However, the correlation with the permeability values is quite good, that is, without significant dispersion, and seems to follow the same trend for the two blocks studied (2) and (3). One value found by the reconstruction (3A1) is very close to the experimental values, but the permeability for the reconstructed sample 2A1 seems to be too high. This shows that for the sandstone studied, an increase in the porosity value is not always followed by an increase of the permeability as is the case with the homogeneous Fontainebleau sandstone.

6.2 Taylor dispersion

Taylor dispersion has been studied for several reconstructed media of sample 2A1. Their characteristics are summarized in Table 6. In all cases, the unit cell of the periodic medium is cubic, with size L. The samples have similar open porosities ε_0. The reduced longitudinal dispersivity $\bar{D}^*_{//}/D$ has been computed for various values of the Peclet number, based on the correlation length $\mathcal{L} = 18$ μm (4). The results are shown in Figure 9. Similar results are obtained for all samples, though the dispersion coefficient may vary over about one order of magnitude for large Peclet numbers. The transition between convection and diffusion occurs between $Pe \approx 10^{-2}$ and $Pe \approx 10^{-1}$. The dependence of $\bar{D}^*_{//}/D$ upon Pe tends to a power-law in all cases, although a slight positive inflection remains in this range of Peclet numbers. The exponent α evaluated from the two last points in Figure 9 ranges from 1.5 to 1.8. There is no obvious correlation

TABLE 6

Reconstructed samples for data set (2A1) used for computing the dispersivity

	N_c	ε_0	L (μm)	K (mD)	$\bar{\sigma}$	α
1	20	0.182	204	213	0.0198	1.61
2	20	0.196	204	207	0.0192	1.47
3	20	0.145	204	280	0.0192	1.68
4	20	0.183	204	72	0.0147	1.80
5	33	0.182	337	163	0.0148	1.71

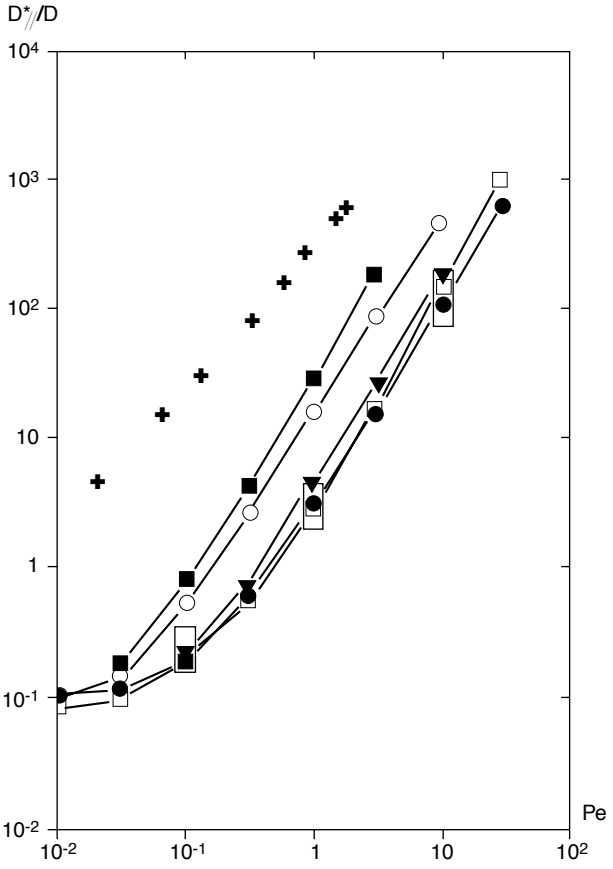

Figure 9

Reduced longitudinal dispersivity $\bar{D}^*_{//}/D$ as a function of the Peclet number $Pe = \mathcal{L}\bar{v}^*/D$. The symbols refer to the reconstructed samples of Vosges sandstone of Table 6 (●, ○, ▼, □ and ■ for samples 1, 2, 3, 4 and 5 respectively) and the vertical bars to the envelop of the data of Sallès *et al.* (1993b) for Fontainebleau sandstone.
Comparison with the experimental values found by displacement of a tracer (+).

between the relative positions of the curves of Figure 9 and the porosity, permeability or conductivity of the corresponding samples.

Again, the present data are compared to corresponding results for Fontainebleau sandstones (Sallès *et al.*, 1993b). The longitudinal dispersivities depicted in Figure 9 were obtained on numerical samples reconstructed with $N_c = 20$, according to various real samples with a wide range of porosities 0.09 to 0.30. They show no obvious sensitivity to the porosity and tend to a power-law of the Peclet number with $\alpha \approx 1.6$. The dispersivity of the present Vosges sandstone is very similar.

It should be kept in mind that owing to the periodicity of the models, these results hold under the assumption that the material is homogeneous at the macroscale. The longitudinal dispersion results in part from the coexistence of low (dead-ends, low permeability zones) and high (main channels) velocity regions in the pore space; hence, part of the solute may be delayed while another part is convected with the largest interstitial velocities. Thus, if the real medium has heterogeneities (such as permeability variations) at a scale larger than the size of the samples used to determine the parameters of the reconstruction, they are not accounted for and dispersion may be underestimated. Physical measurements present the same difficulty. If the dispersivity is measured on blocks too small to encompass a statistically representative sampling of the heterogeneities at the various scales, the same kind of underestimation can arise and the dispersion might even be unable to reach the Gaussian behavior crucial to the description by the dispersion tensor $\bar{\boldsymbol{D}}^*$. Sallès *et al.* (1993b) gave a rough estimate for the minimum size L of a typical sandstone required to establish this Gaussian regime

$$L > Pe/10 \text{ (meters)} \qquad (19)$$

This feature is also ignored by the present simulations, valid for macroscopically homogeneous media and asymptotically long times, but it could be adressed by the Monte Carlo simulations mentioned in Section 5, provided that sufficient geometrical information is available (Sallès *et al.*, 1993b).

6.3 Experimental measurement of dispersion

The longitudinal dispersion has been measured in the lab with the use of a pair of fluids: water containing 30 g/l NaCl and KI as a tracer with the concentration $Co = 25$ ppm. The two fluids are injected the one after the other with different flowrates: from 2 to 180 cm^3/h. The concentration C of the effluent is measured versus time.

The dispersion coefficient has been calculated using:

$$D^*_{/\!/} = 1/2\ \sigma^2\ L\ v^*$$

The curves of the relative concentration C/Co vs time are drawn on a galtonian scale and the quantity σ directly calculated in the central linear parts of the curves. The curves exhibit a good symmetry; the mean value $C/Co = 0.5$ corresponds to the time needed for the injection of one pore volume. The Peclet numbers corresponding to the experimental conditions have also been calculated using:

$$Pe = v^*\ d_p/D$$

v^* is the interstitial velocity, d_p a dimension of the porous medium, and D the molecular diffusivity: $1.865 \times 10^{-5}\ cm^2 s^{-1}$.

A problem arises concerning the value of d_p. In the case of an unconsolidated porous medium, d_p is the grain diameter; however it is more difficult to quantify it in the case of a consolidated sandstone. It is even more difficult when the medium is somewhat heterogeneous.

The calculation of Pe has been performed with d_p as the correlation length used in the theoretical part of the paper, that is $d_p = 18\ \mu m$. The values corresponding to the experimental rates and the points $D^*_{/\!/}/D = f(Pe)$ are shown in Figure 9. The comparison with the theoretical results shows that the experimental values are ten times larger than the values found by reconstruction.

The parameters able to shift our curves contained in $D^*_{/\!/}$ and in Pe are only σ and d_p. For example, if we use a value of d_p ten times higher than the one used previously, that is in the range of 200 microns, the curves fit well. This dimension corresponds to the dimension of a reconstructed sample. It can be seen on the same figure that the experimental results are not too far from those obtained by reconstruction if in this last case the dispersion curve starts, as usual, from a value in the range of 0.7 for low Peclet numbers.

7 SIMULATION OF MERCURY POROSIMETRY EXPERIMENTS

Mercury porosimetry relies on the property of mercury not to wet the materials that constitute most of the natural porous media. Consequently, a pressure P

has to be applied to this fluid to force it to enter a cavity whose throat has a radius R

$$P = 2\,\gamma\cos\theta/R \tag{20}$$

where γ is the surface tension of the mercury and θ is the contact angle. Thus, a throat size distribution spectrum can be obtained by measuring the volume of injected fluid as a function of an imposed pressure. We have developed a numerical algorithm simulating this invasion (Yao, 1994), based on the fact that the domain $V(P)$ reachable by the fluid is supposed to be identical to the one reachable by spherical particles with radius R, related to P by (20).

Again, the medium is represented numerically by a three-dimensional binary array of 0 or 1. We define in the pore space a function $ds(\mathbf{r})$, equal to the distance from $\mathbf{r}$ to the closest solid wall. A sphere with radius R smaller or equal to ds can be inserted at $\mathbf{r}$. This does not mean however that it is actually able to migrate to this location, owing to possible smaller restrictions upstream from $\mathbf{r}$. The volume $V(R)$ is built by using a pseudo-diffusion algorithm, allowing the propagation of a discrete quantity (0/1), starting from one face of the sample, restricted to the domain where ds is larger than R. Note that the simulations do not refer to the interfacial properties σ and θ of the mercury. Only geometrical quantities are handled, and the throat size distribution spectrum is obtained directly, whereas the interpretation of the experimental curves $V(P)$ resorts, generally, to relations like (20), which implicitly consider the medium as a bundle of capillary tubes.

For large R, corresponding via (20) to small pressures, the particle (or the mercury) can possibly penetrate into the sample, but cannot cross it entirely. In this case, a penetration depth $H(R)$ can be defined by dividing the injected volume by the outer area of the sample exposed to the fluid

$$H(R) = \frac{\text{injected volume}}{\text{outer surface}} \tag{21}$$

When the pressure increases, the depth H increases as well until it becomes infinite at a threshold P_c, corresponding to a radius R_c, meaning that the particle is able to cross the whole medium. However, the pore space is not yet totally invaded, and small cavities remain empty. We define the volume fraction of the injected domain $\varepsilon(R)$

$$\varepsilon(R) = \frac{\text{injected volume}}{\text{total volume}} \tag{22}$$

When pressure grows, $\varepsilon(R)$ of course tends toward the porosity $\varepsilon = \varepsilon(0)$ of the sample.

For a given size and shape of the porous sample, it is possible to define $\varepsilon(R)$ in the form (22) on the whole range of radii, although this quantity is not intrinsic to the material since it depends for large R on the ratio surface/volume of the sample.

Simulations have been conducted on a periodic reconstructed sample with $N_c = 55$; the size of the elementary cubes is $a = 6.12\ \mu$m. The dimension of the unit cell of the sample is $(337\ \mu\text{m})^3$, and its porosity is $\varepsilon = 0.162$. The penetration depth $H(R)$ (21) and the volume fraction $\varepsilon(R)$ (22) are presented in Figures 10a and 10b. Percolation occurs for a critical radius $R_c \approx 6\,\mu$m. At this stage, the volume fraction of the invaded domain is $\varepsilon(R_c) \approx 0.10$. The whole pore space is injected for $R \approx 3.06\,\mu$m, which corresponds to the spatial resolution of the discrete representation of the geometry. In order to facilitate comparisons with experimental data, we have built a complete curve $\varepsilon(R)$ on the whole range of R, by assuming that the experimental sample is cubic with a volume of 1 cm^3 (Figure 10c). The highest point in Figure 10a might not be totally reliable since, then, the fluid reaches a depth of the order of the dimension of the unit cell and, thus, finite-size effects are likely to occur. Consequently, the dashed line in Figure 10c is probably closer to reality. This curve is typical of the experimental spectra obtained for sandstones, with a very sharp transition between 3 and 7 μm.

CONCLUSIONS

A combination of simulation and experimental techniques has been used for the study of Vosges sandstone samples. A serial tomography technique has been applied to double pore casts of the samples, and offered a large number of physical sections that were digitized and analyzed geometrically. Random numerical samples were reconstructed using the porosity and autocorrelation function of the thin sections. Stokes flow, ordinary diffusion, dispersion, and mercury intrusion in the simulated structures were studied and permeability, formation factor and dispersivity were calculated and compared to various experimental data. A small degree of anisotropy was revealed from the calculation of the correlation length in the three directions. It was found that the computed values for the permeability and the formation factor are comparable

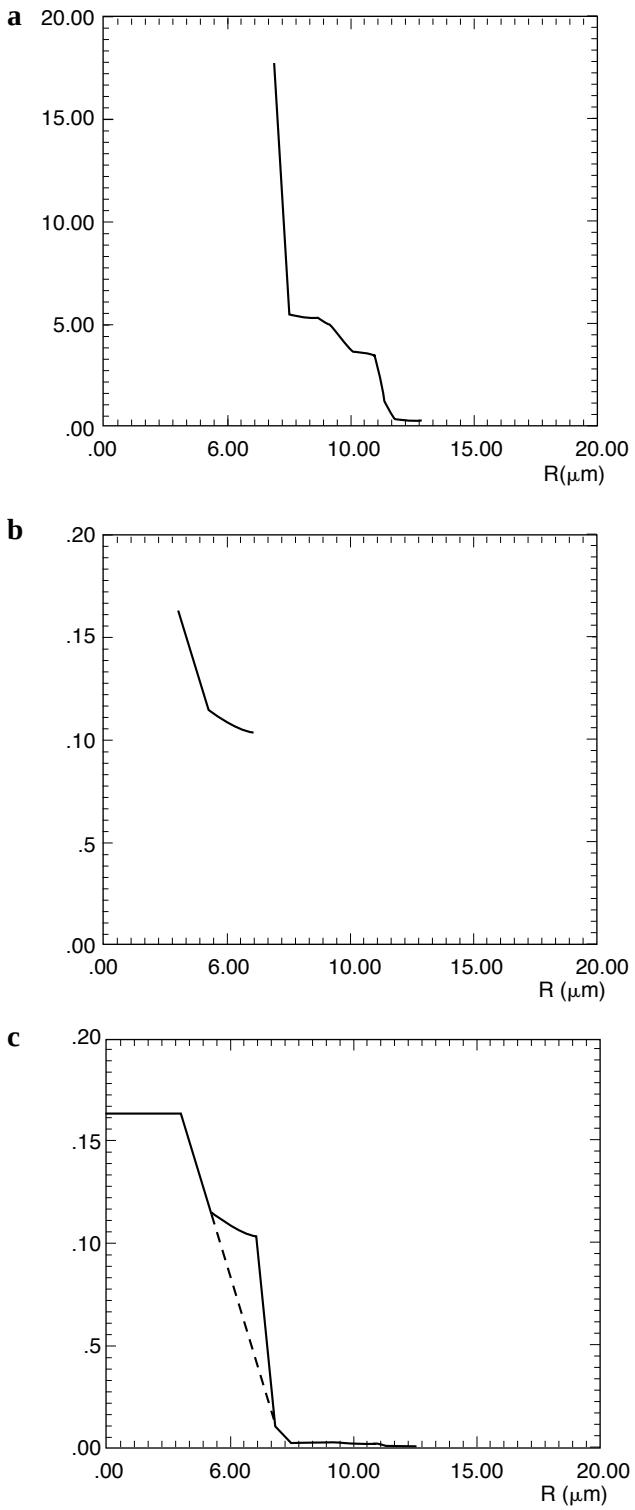

Figure 10

Throat size distribution spectrum computed on a reconstructed sample with $N_c = 55$ and $a = 6.12$ μm. The penetration depth $H(R)$ (21) in mm and the volume fraction $\varepsilon(R)$ (22) are presented in (a) and (b) versus the throat radius R in μm. The complete curve $\varepsilon(R)$ in c assumes that the experimental sample is cubic with a volume 1 cm^3.

to the corresponding values for Fontainebleau sandstone samples analyzed in a similar fashion.

ACKNOWLEDGMENTS

The authors gratefully acknowledge the support of a *Brite Euram Contract BRE2CT92-0191.*

REFERENCES

Adler P.M. (1992), *Porous Media: Geometry and Transports*, Butterworth/ Heinemann, London.

Adler P.M., C.G. Jacquin and J.A. Quiblier (1990), Flow in simulated porous media. *Int. J. Multiphase Fow,* **16**, pp. 691-712.

Adler R.J. (1981), *The Geometry of Random Fields,* Wiley, New York.

Gradshteyn J.P. and I.M. Ryshik (1965), *Table of Integrals Series and Products,* Academic Press, New York.

Joshi M. (1974), A class of stochastic models for porous media. *PhD. Thesis,* University of Kansas, Lawrence, Kansas.

Lemaître R. and P.M. Adler (1990), Fractal porous media. IV-three-dimensional stokes flow through random media and regular fractals. *Transp. Porous Media,* **5**, pp. 325-340.

Lin C. and J. Hamasaki (1983), Pore geometry: a new system for quantitative analysis and 3-D display. *J. Sed. Petrol.,* **53**, pp. 670-672.

Peyret R. and T.D. Taylor (1985), *Computational Methods for Fluid Flow,* Springer-Verlag, Berlin.

Quiblier J.A. (1984), A new three-dimensional modeling technique for studying porous media. *J. Colloid Interf. Sci.,* **98**, pp. 84-102.

Sallès J., J.F. Thovert and P.M. Adler (1993a), Reconstructed porous media and their application to fluid flow and solute transport. *J. Contaminant Hydrology,* **13**, pp. 3-22.

Sallès J., J.F. Thovert, R. Delannay, L. Prévors, J.L. Auriault and P.M. Adler (1993b), Taylor dispersion in porous media. Determination of the dispersion tensor. *Phys. Fluids A,* **5**, pp. 2348-2376.

Straley C. and M.M. Minnis (1983), Epoxy rock replicas for microtoming. *J. Sed. Petrol.,* **53**, pp. 667-669.

Thovert J.F., F. Wary and P.M. Adler (1990), Thermal conductivity of random media and regular fractals. *J. Appl. Phys.,* **68**, pp. 3872-3883.

Yadav G.D., F.A.L. Dullien, I. Chatzis and I.F. Macdonald (1987), Microscopic distribution of wetting and nonwetting phases in sandstones during immiscible displacements. *SPE Reservoir Engineering,* pp. 137-147.

Yao J., P. Frykman, F. Kalaydjian, J.F. Thovert and P.M. Adler (1993), High order moments of the phase function in reconstructed porous media. *J. Colloid Interface Sci.,* **156**, pp. 478-490.

Final manuscript received in September 1996